

# MARFORMER: AN EFFICIENT METAL ARTIFACT REDUCTION TRANSFORMER FOR DENTAL CBCT IMAGES

Yuxuan Shi<sup>1</sup>, Jun Xu<sup>1\*</sup>, and Dinggang Shen<sup>2</sup>

<sup>1</sup>School of Statistics and Data Science, Nankai University

<sup>2</sup>School of Biomedical Engineering, ShanghaiTech University

## ABSTRACT

Cone Beam Computed Tomography (CBCT) plays a key role in dental diagnosis and surgery. However, the metal teeth implants could bring annoying metal artifacts during the CBCT imaging process, interfering diagnosis and downstream processing such as tooth segmentation. In this paper, we develop an efficient Transformer to perform metal artifacts reduction (MAR) from dental CBCT images. The proposed MAR Transformer (MARformer) reduces computation complexity in the multihead self-attention by a new Dimension-Reduced Self-Attention (DRSA) module, based on that the CBCT images have globally similar structure. A Patch-wise Perceptive Feed Forward Network (P2FFN) is also proposed to perceive local image information for fine-grained restoration. Experimental results on CBCT images with synthetic and real-world metal artifacts show that our MARformer is efficient and outperforms previous MAR methods and two restoration Transformers.

## 1 INTRODUCTION

As a useful technology for radiographic imaging, Cone Beam Computed Tomography (CBCT) is widely utilized in oral surgery [1], orthodontics [2], and dental implant [3], etc. High-quality dental CBCT imaging is of great importance to guarantee accurate clinical diagnosis. However, the metal teeth implants would bring unpleasant metal artifacts like flare during the imaging process due to the radiation scattering and beam hardening effects [4]. These artifacts will somewhat damage the post-processing diagnosis-related tasks like tooth segmentation. For example, in Fig. 1, we present two CBCT images with or without flare artifacts contaminated by metals in teeth. The two images are segmented by a segmentation network [5] trained on large scale tooth CBCT images with accurate masks annotated by experienced dentists. One can see that, the CBCT image with metal artifacts are inaccurately segmented with heavy missing of teeth area, which cannot be used to infer the teeth structure. To this end, it is essential to remove the metal artifacts on the dental CBCT images with metal implants for the following usage of tooth segmentation in clinical diagnosis.

During the past decades, many metal artifact reduction (MAR) methods are developed, which can be roughly categorized into sinogram completion methods [6, 7, 8, 9], optimization based methods [10, 11, 12], and data driven methods [13, 14, 15, 16, 17, 18]. Sinogram completion methods mainly project CBCT images into the sinogram domain and then complete the corresponding metal influenced area via interpolation [6, 7, 8, 9]. Optimization based methods [10, 11, 12] model the MAR process as proper objective functions and reconstruct the clean CBCT images by optimization algorithms like ADMM [19]. Data driven methods usually perform MAR by learning deep neural networks on paired clean and MA degraded CBCT images [13, 14, 15, 16, 17, 18].

Despite achieving promising MAR performance, most existing deep MAR networks built upon convolutional neural networks (CNNs) are usually difficult to capture global correlation of metal artifacts in a CBCT image. A natural alternative is to develop Transformers for better MAR performance. By mak-

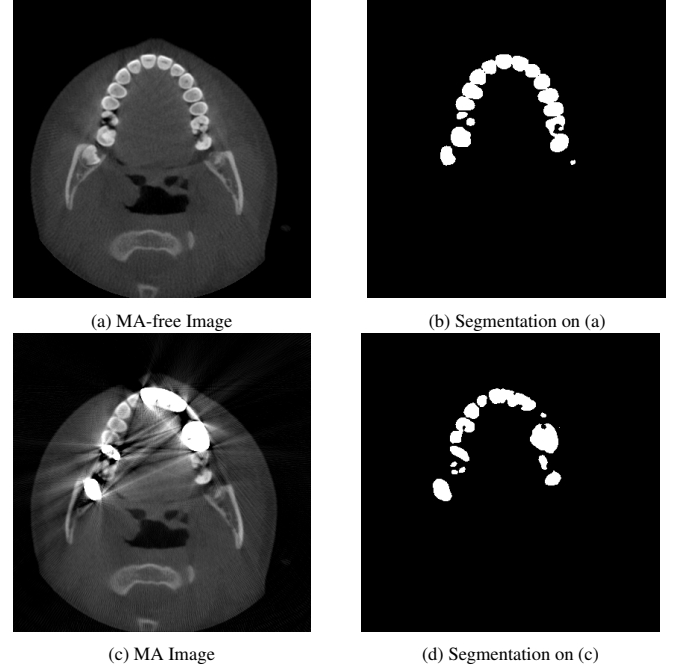
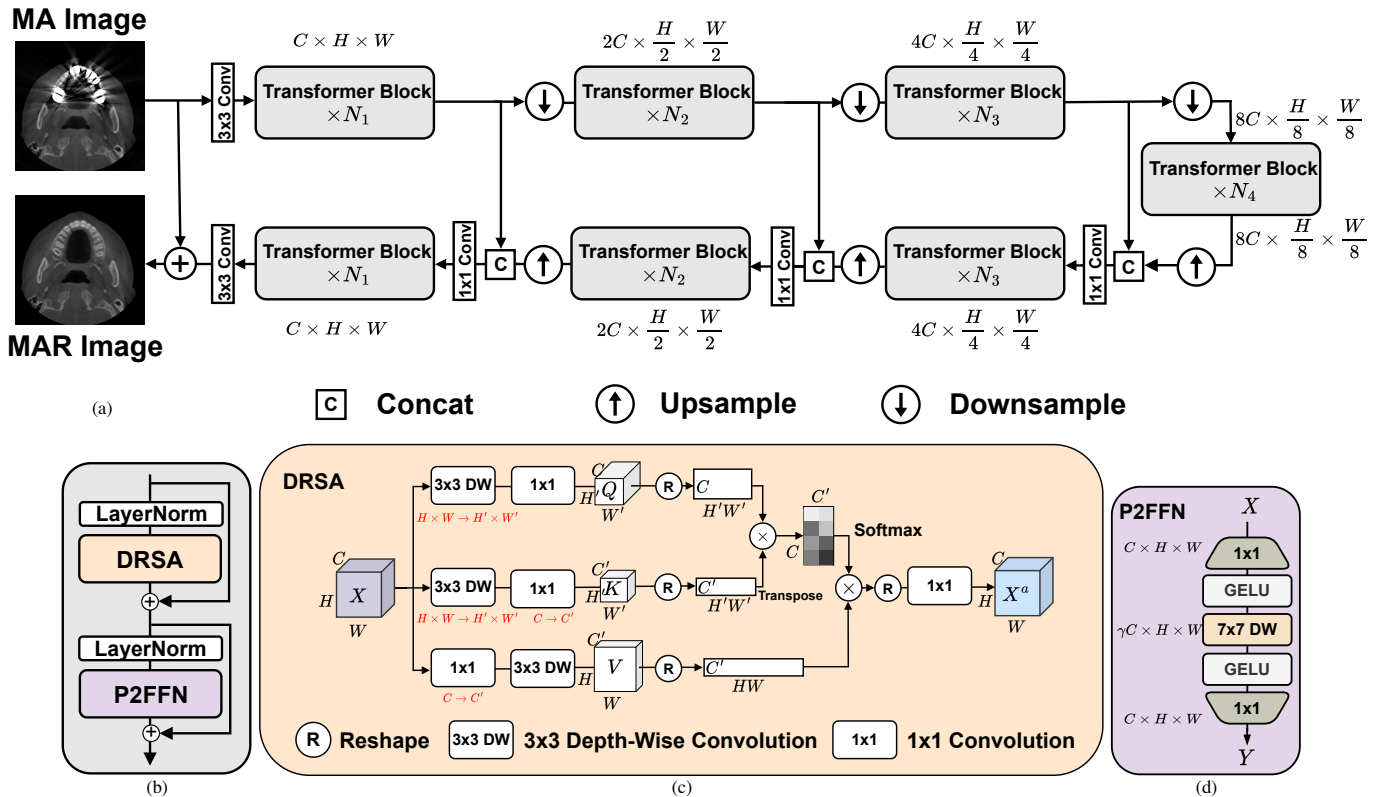


Figure 1: Segmentation results by Poolformer [5]. (a) A CBCT image without metal artifacts. (b) Segmentation mask of Poolformer on (a). (c) The image (a) with synthetic metal artifacts. (d) Segmentation mask of Poolformer on (c).

ing better usage of global dependency [20], Transformers have outperformed CNNs on many tasks ranging from pattern recognition [21] to image restoration [22, 23]. However, Transformer based models are usually parameter-demanding and computationally expensive [21, 24, 22]. To alleviate these problems, the token-wise learning scheme is developed in ViT [21]. But this also reduces the correlation field of self-attention from global image to local patches, limiting the MAR performance. To this end, it is essential to develop an efficient and light-weight Transformer model that is feasible to exploit global correlation



information for effective CBCT MAR.

With the rise of deep learning, several convolutional neural network (CNN) models have been proposed for MAR. Some operate purely in the image domain [28, 13], while others complete the sinogram before reconstruction [15] or use dual domain approaches [16, 17, 18, 29]. Most existing deep MAR methods use CNN architectures. Recently, transformers have shown promising effect for restoration tasks [30, 23, 22], but the high computation occupation of the model blocks their application. To overcome this problem, we employs a light-weight transformer model that has the similar computation cost with CNN models and shows remarkable performance on MAR task.

## 2.2 Efficient Vision Transformers

Recently, transformers have been applied to image restoration tasks [30, 22, 23]. [30] utilizes the Swin Transformer [31] for

## 2 RELATED WORK

Existing metal artifact reduction methods could be categorized into traditional sinogram completion, iterative reconstruction, and deep learning based medical image restoration. Early sinogram completion methods rely on interpolating the missing

restoration. Restormer [22] and Uformer [23] employ U-Net like structures and demonstrate efficient computation for image restoration task. Vision transformers mainly compute self-attention across spatial dimensions, incurring high cost due to the quadratic computation complexity of the similarity matrix in the self-attention part. Similar to [22] which is able to handle high resolution image, we compute self-attention across channels, since the number of channels is less than spatial size for restoration task. Furthermore, we introduce dimension reduction method in the transformer block to cut computation costs in both channel and spatial dimensions.

### 3 PROPOSED MARFORMER FOR DENTAL CBCT IMAGE MAR

#### 3.1 Network Overview

As shown in Fig. 2, the proposed MARformer utilizes a U-net architecture with three-level hierarchical encoder-decoders and the  $i$ -th ( $i = 1, 2, 3$ ) level of encoder-decoder contains  $N_i$  transformer blocks, together with a bottleneck including  $N_4$  transformer blocks. Each transformer block is consisted of the proposed Dimension-Reduced Self-Attention (DRSA) module and the Patch-wise Perceptive Feed Forward Network (P2FFN), as shown in Fig. 2 (b).

Given an input dental CBCT image degraded by metal artifacts  $\mathbf{I} \in \mathbb{R}^{H \times W}$ , we first extract initial image feature  $\mathbf{X}_0 \in \mathbb{R}^{C \times H \times W}$  by a  $3 \times 3$  convolution. Then the image feature  $\mathbf{X}_0$  is fed into the 1-st level encoder. The output feature is spatial-wise downsampled and channel-wise expanded to a size of  $2C \times \frac{H}{2} \times \frac{W}{2}$ . The resulting feature map is further fed into the 2-nd level encoder. After three levels of hierarchical encoders, the output feature map of size  $8C \times \frac{H}{8} \times \frac{W}{8}$  is input to the bottleneck. In the decoder stage, the feature map is spatial-wise upsampled and channel-wise shrunk by half in each level of decoder, and concatenated with the feature output by the corresponding-level encoder. To keep the channel dimension consistent between different levels, we use a  $1 \times 1$  convolution to reduce the dimension of the concatenated feature from  $2C$  to  $C$  before it is fed into the next-level decoder. The downsample and upsample operations between different levels of encoder or decoders are implemented by pixel unshuffle/shuffle operations [37]. The feature map after the last decoder is fused by a  $3 \times 3$  convolution to get the image residual  $\mathbf{R} \in \mathbb{R}^{H \times W}$ , which is added to the input image  $\mathbf{I}$  to produce the final MAR image  $\hat{\mathbf{I}} = \mathbf{I} + \mathbf{R}$ .

#### 3.2 Components of the Transformer Block

In our MARformer, each transformer block is consisted of a Dimension-Reduced Self-Attention (DRSA) module and a Patch-wise Perceptive Feed Forward Network (P2FFN), as shown in Fig. 2 (b).

**Dimension Reduced Self-Attention (DRSA).** The goal of the proposed DRSA module is to perform efficient self-attention on high-resolution feature maps. Given an input feature  $\mathbf{X} \in \mathbb{R}^{C \times H \times W}$ , we compute global similarity matrix [20, 21] along the channel dimension, instead of spatial dimension [20, 21]. Assume that there is only one head of self-attention, our DRSA module first projects the input feature  $\mathbf{X}$  into spatially-reduced query component  $\mathbf{Q} \in \mathbb{R}^{C' \times H' \times W'}$  ( $H' < H$ ,  $W' < W$ ), key compo-

nent  $\mathbf{K} \in \mathbb{R}^{C' \times HW}$ , and value component  $\mathbf{V} \in \mathbb{R}^{C' \times HW}$  ( $C' < C$ ). The projection is implemented by a  $1 \times 1$  convolution and a  $3 \times 3$  depth-wise convolution, as plotted in Fig. 2 (c). For example, the spatial downsampling is realized by  $3 \times 3$  convolutions with a stride larger than 1 (e.g., 2) while the channel downsampling is realized by  $1 \times 1$  convolutions. Then the DRSA is performed as  $\text{Attention} = \text{Softmax}(\frac{1}{\alpha} \mathbf{Q} \mathbf{K}^T) \mathbf{V}$ , where “Softmax” is the softmax normalization operation and  $\alpha$  is a learnable scalar parameter.

In our DRSA, since the image size  $HW$  is usually much larger than the channel dimension  $C$ , the computational complexity of calculating the similarity matrix along the channel dimension is  $O(CC'H'W' + CC'HW)$ , which is smaller than the computational complexity by calculating spatial-wise similarity matrix, i.e.,  $O(C(HW)^2)$ , when projecting the input feature  $\mathbf{X}$  onto feature maps of  $\mathbf{Q}, \mathbf{K}, \mathbf{V} \in \mathbb{R}^{HW \times C}$ . Besides, calculating channel-wise similarity matrix is also able to enable our MARformer to exploit global correlation information for effective dental CBCT image MAR. We also split the channel dimension into multiple groups to perform multi-head self-attention.

**Patch-wise Perceptive Feed Forward Network (P2FFN).** As is shown in Fig. 2 (d), our P2FFN is consisted of a  $1 \times 1$  convolution to expand the channel dimension from  $C$  to  $\gamma C$ , a GELU activation function [38], a depth-wise  $p \times p$  convolution with a GELU to perceive local image information that is important to image restoration tasks, and another  $1 \times 1$  convolution to shrink the channel dimension from  $\gamma C$  to  $C$ . Finally, we add a skip connection with the input feature to the end of P2FFN to improve the learning capability of our MARformer.

#### 3.3 Implementation details

The  $k$ -th level ( $k = 1, 2, 3$ ) of the encoder-decoder in our MARformer contains  $N_k$  transformer blocks, and the bottleneck contains  $N_4$  transformer blocks. The numbers of heads when calculating the similarity matrices in transformer blocks at different levels of encoder-decoders are denoted as  $H_1, H_2, H_3, H_4$ . The spatial and channel downsample ratio  $r$  are both set as 2. We set the channel dimension  $C = 48$  and the expansion factor  $\gamma = 2$  in P2FFN.

We implement three models of our MARformer with different parameter amounts. For the largest one, denoted as MARformer-L, we set  $N_1 = 1, N_2 = 2, N_3 = 4, N_4 = 8$  and  $H_1 = 1, H_2 = 2, H_3 = 4, H_4 = 8$ . For the baseline one, denoted as MARformer-B, we set  $N_1 = 1, N_2 = 2, N_3 = 3, N_4 = 4$  and  $H_1 = 1, H_2 = 2, H_3 = 4, H_4 = 8$ . For the tiny one, denoted as MARformer-T, we set  $N_1 = 1, N_2 = 2, N_3 = 3, N_4 = 4, H_1 = H_2 = H_3 = H_4 = 1$ , and fix the channel dimension as 48 in all levels of encoder-decoders and the bottleneck.

## 4 EXPERIMENTAL RESULTS

### 4.1 Dataset Preparation

To evaluate different methods on metal artifacts removal, we collected 263 CBCT scans, each of which contains 224 to 448 slice images at a resolution of  $0.4\text{mm} \times 0.4\text{mm}$ ,  $0.3\text{mm} \times 0.3\text{mm}$ , or  $0.25\text{mm} \times 0.25\text{mm}$  from over ten stomatological hospitals. The values of CT slices are clipped between  $-1,000\text{HU}$  and  $2,800\text{HU}$ , and then converted to attenuation coefficients. By

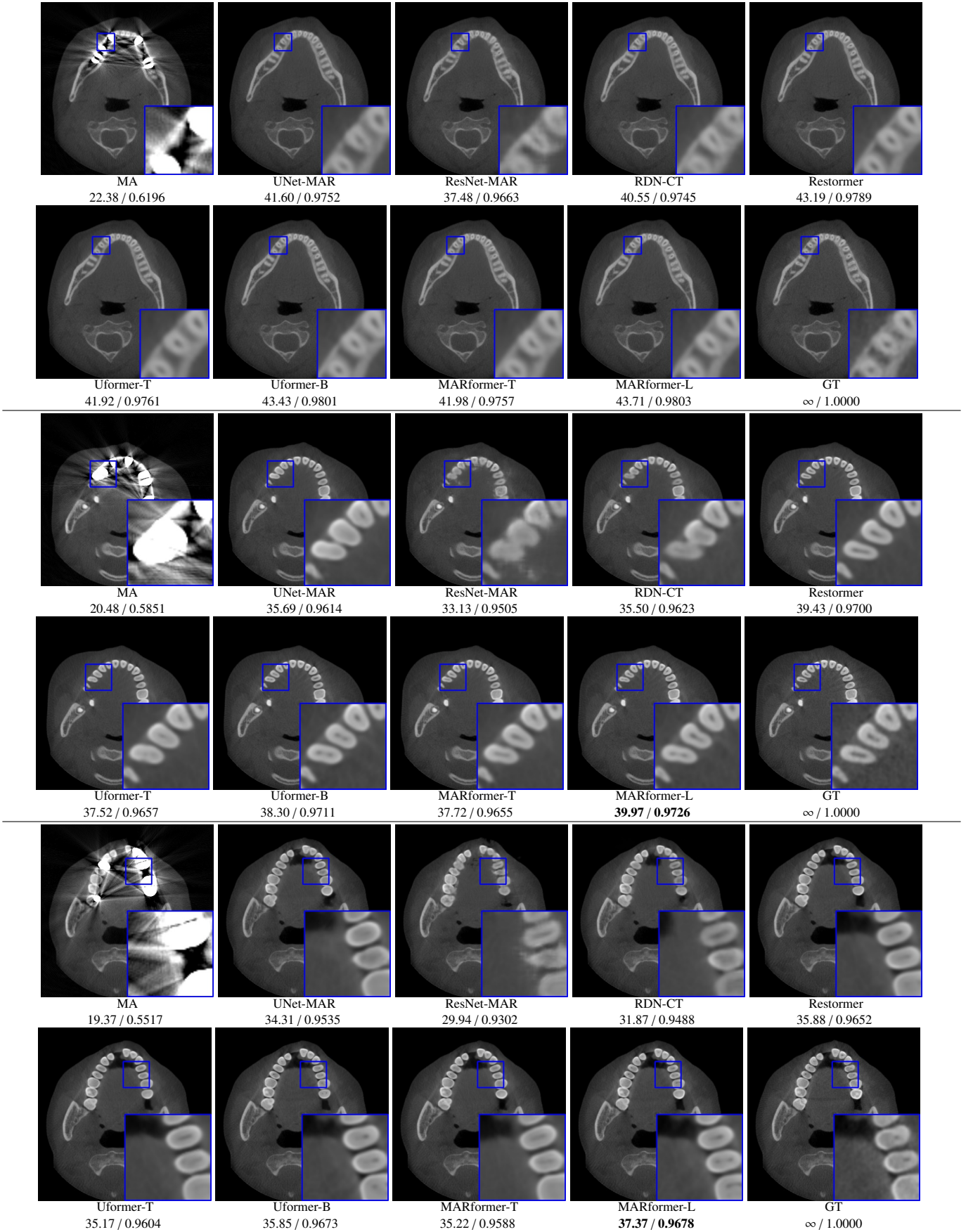


Figure 3: Visual comparison of MAR images by different methods on synthetic MA image. The PSNR (dB)/SSIM results are reported below each image for reference.

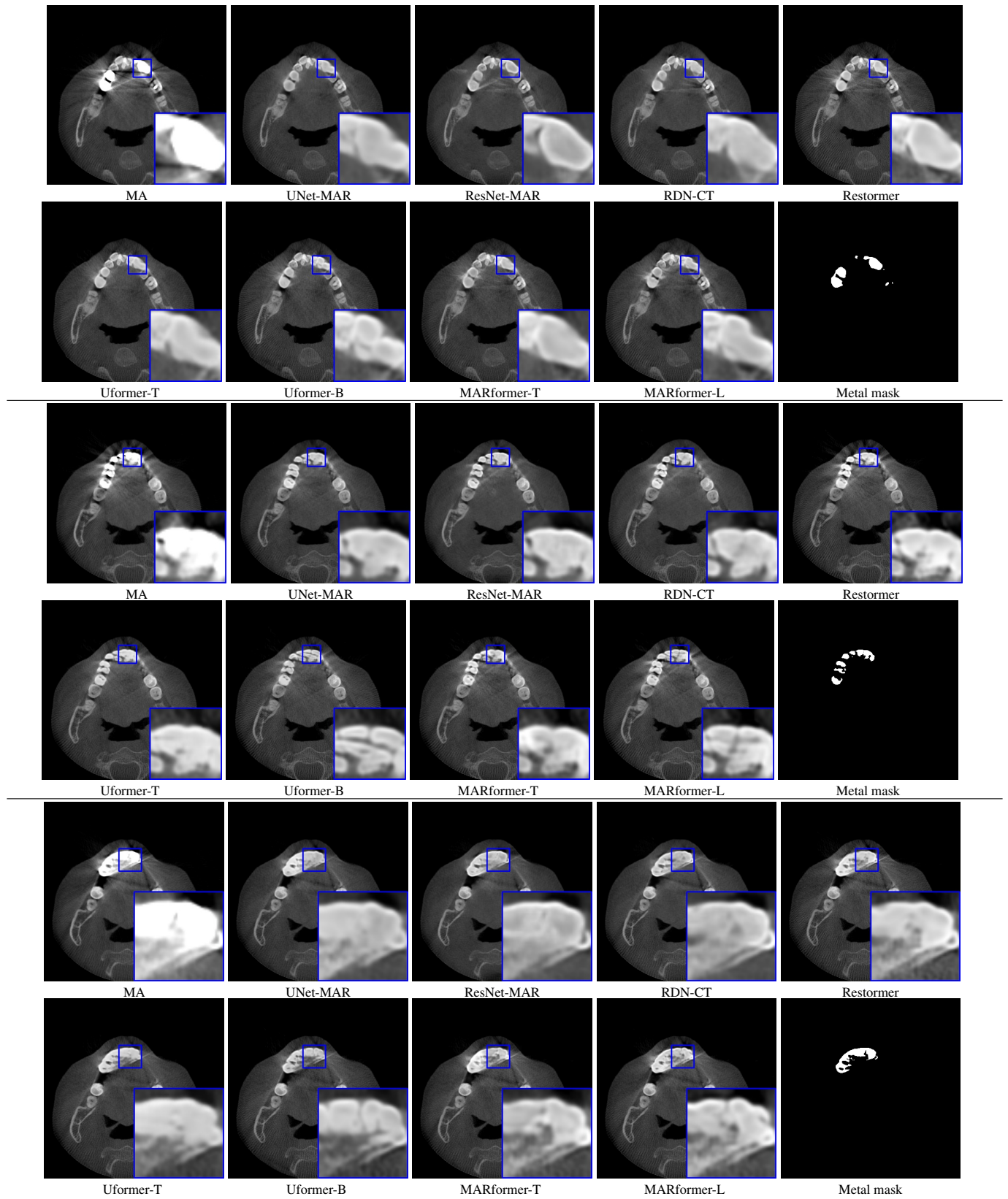


Figure 4: Comparison of MAR images by different methods on real-world MA image. The last image is the metal mask by selecting the pixel area over 2800HU in the MA image.

Table 1: **Quantitative results of PSNR (dB), SSIM [36] and Dice score over the synthesized MA dataset.** The FLOPs and speed are test on a single  $400 \times 400$  image. “-” means that the result is not available. “\*” means that the method is test on an Intel Xeon Gold 6348 CPU. The best results are highlighted in **bold**.

Method	PSNR	SSIM	Dice	Params(M)	FLOPs(G)	Speed(ms)
Input MA Images	25.72	0.7207	0.6443	-	-	-
LI	28.66	0.8822	0.6868	-	-	75*
NMAR	28.93	0.9023	0.6963	-	-	269*
CNNMAR	30.05	0.9391	0.7511	-	-	373*
UNet-MAR	40.20	0.9707	0.7983	12.25	44.28	<b>10</b>
ResNet-MAR	37.34	0.9626	0.7744	0.59	95.34	18
RDN-CT	39.68	0.9711	0.7929	13.76	2200.88	256
Restormer	42.73	0.9777	0.8014	26.12	377.72	208
Uformer-B	42.98	<b>0.9790</b>	<b>0.8041</b>	50.42	205.82	116
Uformer-S	42.35	0.9770	0.8039	20.66	95.84	90
Uformer-T	41.44	0.9744	0.8024	5.24	25.39	51
<b>MARformer-L</b>	<b>43.11</b>	0.9789	0.8031	11.76	60.25	48
<b>MARformer-B</b>	42.89	0.9782	0.8021	6.88	46.20	36
<b>MARformer-T</b>	41.40	0.9736	0.8011	<b>0.40</b>	<b>12.82</b>	31

taking the slices containing 10 or more pixels over 2,800HU CT values as metal artifact degraded images, we extract 21,625 clean slice images and 9,834 metal artifact (MA) degraded slice images from these CBCT scans. Then we resize the extracted slice images to  $400 \times 400$  resolutions. Each clean CBCT slice is manually annotated with accurate tooth segmentation masks by experienced dentists. For model training and evaluation, we employ the method in [17] to simulate MA degraded images by randomly selecting the annotated segmentation masks as metal implants. We randomly select 17,429 pairs of clean and MA degraded images from 210 scans as the training set, 391 pairs of images from 5 scans as the validation set, and 3,805 pairs of images from 48 scans as the test set.

#### 4.2 Training and Evaluation Details

**Training.** We train the three MARformers (L/B/T) for 300 epochs with a batch size of 8, by Adam optimizer with  $\beta_1 = 0.9$  and  $\beta_2 = 0.99$ , under an  $\ell_1$  loss function. The learning rate periodically starts from  $10^{-3}$  and decayed to  $10^{-7}$  in 30 epochs via cosine annealing decay scheme [39]. We perform all experiments using the Pytorch framework [40] on two NVIDIA Tesla V100 32GB GPUs.

**Evaluation.** We calculate the average Peak Signal Noise Ratio (PSNR) and Structural Similarity (SSIM) [36] to evaluate the quantitative MAR results of comparison methods on the MA degraded images in the test set. We also employ the Poolformer [5], trained on the 17,429 clean slices with annotated masks [5], to perform tooth semantic segmentation on the MAR images restored by our MARformer-L. We use the Dice score to evaluate the segmentation results.

#### 4.3 Comparison Results

**Comparison methods.** To evaluate the effectiveness and efficiency of the proposed MARformers, we compare four representative MAR methods, *i.e.*, LI [6], NMAR [8], RDN-CT [17], CNNMAR [16], and two image restoration Transformers, *i.e.*, Restormer [22] and Uformer [23]. The three models of Uformer, *i.e.*, Uformer-B/S/T are all used here. The window size of the

Uformer models is set to 5 to fit the input image size. We also evaluate the popular UNet [41] and ResNet [42] with the output head revised to suit for the MAR task, denoted as UNet-MAR and ResNet-MAR, respectively. Here, UNet-MAR has 4 levels of encoder-decoders with 1, 2, 3, 4 convolution blocks (each of which contains a  $3 \times 3$  conv, a BN and a ReLU), respectively. The ResNet-MAR is consisted of 8 residual blocks [42] with feature channel fixed as 64. These modifications ensure that UNet and RDN-CT have comparable parameters with the MARformer-L and MARformer-T, respectively. All comparison methods are retrained on our training set to achieve their best performance on the validation set.

**Results on synthetic MAR.** In Table 1, we provide the quantitative results. One can see that our MARformer-L outperforms the other methods in terms of PSNR and SSIM, but needs only 11.76M parameters and 60.25G FLOPs. Note that the second best method Uformer-B has 50.42M parameters and 205.82G FLOPs. Besides, our MARformer-T achieves similar PSNR and SSIM results with Uformer-T, but needs only 0.40M parameters and 12.82G FLOPs compared to 5.24M and 25.39G for Uformer-T. Our MARformers also achieves faster inference speeds than the Uformers, though with inferior Dice scores, respectively. The qualitative results of visual quality are presented in Fig. 3. We observe that our MARformer-L well recovers the teeth shapes and obtains higher PSNR and SSIM results than the other comparison methods. The light-weight MARformer-L achieves similar results to Uformer-T. All these results validate that our MARformer is more efficient than the comparison methods on dental CBCT MAR.

**Results on real-world MAR.** We also compare these methods on dental CBCT images with real-world metal artifacts. The visual results on one sample are shown in Fig. 4. We observe that our MARformer-T and MARformer-L well separate the adjacent teeth and retain their shapes. This shows that our MARformers, though trained on synthetic data, are effective on real-world MAR.

Table 2: **Quantitative results of PSNR (dB), SSIM [36] and Dice score our MARformer-L with different downsample ratios in the DRSA module.** “baseline” means the DRSA without downsampling the spatial and channel dimension. “S↓ $r$ ” or “C↓ $r$ ” indicate spatial or channel downsampling with a ratio of  $r$ , respectively. The FLOPs are computed on a single 400×400 image as input.

Variant	0	1	2	3	4	5	6	7
Description	MA	baseline	S↓2	C↓2	S↓2 C↓2	S↓4 C↓4	S↓8 C↓8	S↓16 C↓16
PSNR	25.72	43.04	43.09	43.13	43.11	43.10	43.01	42.92
SSIM	0.7207	0.9787	0.9788	0.9788	0.9789	0.9788	0.9786	0.9784
Dice	0.6443	0.8030	0.8019	0.8015	0.8031	0.8025	0.8031	0.8004
Params(M)	-	13.30	13.30	11.76	11.76	10.99	10.61	10.42
FLOPs(G)	-	82.00	67.17	71.06	60.25	54.60	52.63	51.80

Table 3: **Quantitative results of PSNR (dB), SSIM, and Dice score by our MARformer-L, with varying kernel size  $p$  of depth-wise convolution (a) and  $\gamma$  (b) in the P2FFN module.** The FLOPs are computed on a single 400×400 image as input. The comparison is made with the setting  $p = 7$  and  $\gamma = 2$ .

(a) Study of kernel size  $p$ .

Variant	$p$	PSNR	SSIM	Dice	Params(M)	Flops(G)
1	3	42.72	0.9777	0.8030	<b>11.46</b>	<b>55.95</b>
2	5	42.99	0.9784	0.8020	11.52	57.67
3	7	<b>43.11</b>	<b>0.9789</b>	<b>0.8031</b>	11.76	60.25
4	9	43.01	0.9788	0.8027	12.09	63.69

(b) Study of expansion factor  $\gamma$ .

Variant	$\gamma$	PSNR	SSIM	Dice	Params(M)	Flops(G)
5	1	42.81	0.9779	0.8008	<b>8.48</b>	<b>41.39</b>
6	2	43.11	0.9789	<b>0.8031</b>	11.76	60.25
7	3	43.20	0.9792	0.8016	15.04	79.10
8	4	<b>43.28</b>	<b>0.9795</b>	0.8027	18.32	97.96

#### 4.4 Ablation Study

To further analyze the effect of DRSA and P2FFN module, we analyze the main variant of the proposed DRSA and P2FFN modules in our MARformer-L for the MAR of dental CBCT image. The main variant

**Dowsample ratio in our DRSA.** To study the role of spatial and channel downsampling in our DRSA, we develop a baseline of our MARformer without downsampling the spatial or channel dimension in DRSA, and variants with other dowsample ratios of  $r = 4, 8, 16$ . The comparison results are shown in Table 2. From the variants 1 and 3, our MARformer-L needs less parameters by reducing the channel dimension. By downsampling both the spatial and channel dimensions at a ratio of 2, our MARformer-L achieves slightly better performance with less parameter amount and computational costs (FLOPs). By further increasing the downsample ratio  $r = 4, 8, 16$ , the performance of our MARformer-L suffers from slightly performance drop in terms of PSNR and SSIM. This demonstrates that our MARformer-L requires less parameters and computational costs (FLOPs), while being robust to the spatial or channel dimension downsampling.

**Kernel size of the depth-wise convolution and the expansion factor in P2FFN.** To study the varying factor of P2FFN, we study the varying kernel size  $p$  of the depth-wise convolution and the expansion ratio  $\gamma$ . Results are listed in Table 3. (a) The increase of kernel size first positively affects the restoring effectiveness, but then exhibits a subsequent decline effect. (b) While the rise of  $\gamma$  holds considerable significance, it concurrently leads to a substantial growth in both the number of parameters and the computational complexity. It is observed that our MARformer-L obtains the best PSNR, SSIM, and Dice score results with kernel size  $p = 7$ . Besides, our MARformer-L obtains higher PSNR and SSIM results as  $\gamma$  inceases, but suffering from more parameters and computation FLOPs. We set

$\gamma = 2$  to balance the model complexity and performance.

## 5 CONCLUSION

In this paper, we proposed an efficient MARformer for metal artifacts reduction on dental CBCT images. This is achieved by designing a new Dimension-Reduced Self-Attention (DRSA) module to reduce the computational complexity of the self-attention in Transformers. Besides, we also developed a useful Patch-wise Perceptive Feed Forward Network (P2FFN) to perceive local image information for detail reconstruction. Experiments on a large-scale dataset containing CBCT images with synthetic and real-world metal artifacts demonstrate that, our MARformer outperforms the state-of-the-art MAR methods and two image restoration Transformers on both objective metrics and visual quality.

## ACKNOWLEDGMENTS

This work was partially supported in part by National Natural Science Foundation of China (No. 62002176 and 62176068), and the Open Research Fund (No. B10120210117-OF03) from the Guangdong Provincial Key Laboratory of Big Data Computing, The Chinese University of Hong Kong, Shenzhen.

## REFERENCES

- [1] Robert Weiss and Andrew Read-Fuller. Cone beam computed tomography in oral and maxillofacial surgery: an evidence-based review. *Dentistry journal*, 7(2):52, 2019.
- [2] SD Kapila and JM Nervina. Cbct in orthodontics: assessment of treatment outcomes and indications for its use. *Dentomaxillofacial radiology*, 44(1):20140282, 2015.

- [3] Young-Dai Song, Sang-Ho Jun, and Jong-Jin Kwon. Correlation between bone quality evaluated by cone-beam computerized tomography and implant primary stability. *International Journal of Oral & Maxillofacial Implants*, 24(1), 2009.
- [4] Andre Mouton, Najla Megherbi, Katrien Van Slambrouck, Johan Nuyts, and Toby P Breckon. An experimental survey of metal artefact reduction in computed tomography. *Journal of X-ray Science and Technology*, 21(2):193–226, 2013.
- [5] Weihao Yu, Mi Luo, Pan Zhou, Chenyang Si, Yichen Zhou, Xinchao Wang, Jiashi Feng, and Shuicheng Yan. Metaformer is actually what you need for vision. In *Proceedings of the IEEE/CVF conference on computer vision and pattern recognition*, pages 10819–10829, 2022.
- [6] Willi A Kalender, Robert Hebel, and Johannes Ebersberger. Reduction of ct artifacts caused by metallic implants. *Radiology*, 164(2):576–577, 1987.
- [7] Shiyang Zhao, Kyongtae T Bae, Bruce Whiting, and Ge Wang. A wavelet method for metal artifact reduction with multiple metallic objects in the field of view. *Journal of X-ray Science and Technology*, 10(1-2):67–76, 2002.
- [8] Esther Meyer, Rainer Raupach, Michael Lell, Bernhard Schmidt, and Marc Kachelrieß. Normalized metal artifact reduction (nmar) in computed tomography. *Medical physics*, 37(10):5482–5493, 2010.
- [9] Yi Zhang, Yi-Fei Pu, Jin-Rong Hu, Yan Liu, and Ji-Liu Zhou. A new ct metal artifacts reduction algorithm based on fractional-order sinogram inpainting. *Journal of X-ray science and technology*, 19(3):373–384, 2011.
- [10] Ge Wang, Donald L Snyder, Joseph A O’Sullivan, and Michael W Vannier. Iterative deblurring for ct metal artifact reduction. *IEEE transactions on medical imaging*, 15(5):657–664, 1996.
- [11] Xiaomeng Zhang, Jing Wang, and Lei Xing. Metal artifact reduction in x-ray computed tomography (ct) by constrained optimization. *Medical physics*, 38(2):701–711, 2011.
- [12] Catherine Lemmens, David Faul, and Johan Nuyts. Suppression of metal artifacts in ct using a reconstruction procedure that combines map and projection completion. *IEEE transactions on medical imaging*, 28(2):250–260, 2008.
- [13] Jianing Wang, Yiyuan Zhao, Jack H Noble, and Benoit M Dawant. Conditional generative adversarial networks for metal artifact reduction in ct images of the ear. In *International Conference on Medical Image Computing and Computer-Assisted Intervention*, pages 3–11. Springer, 2018.
- [14] Haofu Liao, Wei-An Lin, S Kevin Zhou, and Jiebo Luo. Adn: artifact disentanglement network for unsupervised metal artifact reduction. *IEEE Transactions on Medical Imaging*, 39(3):634–643, 2019.
- [15] Muhammad Usman Ghani and W Clem Karl. Fast enhanced ct metal artifact reduction using data domain deep learning. *IEEE Transactions on Computational Imaging*, 6:181–193, 2019.
- [16] Yanbo Zhang and Hengyong Yu. Convolutional neural network based metal artifact reduction in x-ray computed tomography. *IEEE transactions on medical imaging*, 37(6):1370–1381, 2018.
- [17] Wei-An Lin, Haofu Liao, Cheng Peng, Xiaohang Sun, Jingdan Zhang, Jiebo Luo, Rama Chellappa, and Shao-hua Kevin Zhou. Dudonet: Dual domain network for ct metal artifact reduction. In *Proceedings of the IEEE/CVF Conference on Computer Vision and Pattern Recognition*, pages 10512–10521, 2019.
- [18] Tao Wang, Wenjun Xia, Yongqiang Huang, Huaqiang Sun, Yan Liu, Hu Chen, Jiliu Zhou, and Yi Zhang. Dual-domain adaptive-scaling non-local network for ct metal artifact reduction. In *International Conference on Medical Image Computing and Computer-Assisted Intervention*, pages 243–253. Springer, 2021.
- [19] Stephen Boyd, Neal Parikh, Eric Chu, Borja Peleato, Jonathan Eckstein, et al. Distributed optimization and statistical learning via the alternating direction method of multipliers. *Foundations and Trends® in Machine learning*, 3(1):1–122, 2011.
- [20] Ashish Vaswani, Noam Shazeer, Niki Parmar, Jakob Uszkoreit, Llion Jones, Aidan N Gomez, Łukasz Kaiser, and Illia Polosukhin. Attention is all you need. *Advances in neural information processing systems*, 30, 2017.
- [21] Alexey Dosovitskiy, Lucas Beyer, Alexander Kolesnikov, Dirk Weissenborn, Xiaohua Zhai, Thomas Unterthiner, Mostafa Dehghani, Matthias Minderer, Georg Heigold, Sylvain Gelly, et al. An image is worth 16x16 words: Transformers for image recognition at scale. *arXiv preprint arXiv:2010.11929*, 2020.
- [22] Syed Waqas Zamir, Aditya Arora, Salman Khan, Munawar Hayat, Fahad Shahbaz Khan, and Ming-Hsuan Yang. Restormer: Efficient transformer for high-resolution image restoration. In *CVPR*, 2022.
- [23] Zhendong Wang, Xiaodong Cun, Jianmin Bao, Wengang Zhou, Jianzhuang Liu, and Houqiang Li. Uformer: A general u-shaped transformer for image restoration. In *Proceedings of the IEEE/CVF Conference on Computer Vision and Pattern Recognition*, pages 17683–17693, 2022.
- [24] Yufei Xu, Qiming Zhang, Jing Zhang, and Dacheng Tao. Vitae: Vision transformer advanced by exploring intrinsic inductive bias. *Advances in Neural Information Processing Systems*, 34:28522–28535, 2021.
- [25] Ge Wang, Michael W Vannier, and Ping-Chin Cheng. Iterative x-ray cone-beam tomography for metal artifact reduction and local region reconstruction. *Microscopy and microanalysis*, 5(1):58–65, 1999.
- [26] Abolfazl Mehranian, Mohammad Reza Ay, Arman Rahmim, and Habib Zaidi. X-ray ct metal artifact reduction using wavelet domain  $l_{\{0\}}$  sparse regularization. *IEEE transactions on medical imaging*, 32(9):1707–1722, 2013.
- [27] Zhiqian Chang, Dong Hye Ye, Somesh Srivastava, Jean-Baptiste Thibault, Ken Sauer, and Charles Bouman. Prior-guided metal artifact reduction for iterative x-ray computed tomography. *IEEE transactions on medical imaging*, 38(6):1532–1542, 2018.

- [28] Shiyu Xu and Hao Dang. Deep residual learning enabled metal artifact reduction in ct. In *Medical Imaging 2018: Physics of Medical Imaging*, volume 10573, page 105733O. International Society for Optics and Photonics, 2018.
- [29] Hong Wang, Yuexiang Li, Haimiao Zhang, Jiawei Chen, Kai Ma, Deyu Meng, and Yefeng Zheng. Indudonet: An interpretable dual domain network for ct metal artifact reduction. In *International Conference on Medical Image Computing and Computer-Assisted Intervention*, pages 107–118. Springer, 2021.
- [30] Jingyun Liang, Jiezhong Cao, Guolei Sun, Kai Zhang, Luc Van Gool, and Radu Timofte. Swinir: Image restoration using swin transformer. In *2021 IEEE/CVF International Conference on Computer Vision Workshops (ICCVW)*, pages 1833–1844, 2021. doi: 10.1109/ICCVW54120.2021.00210.
- [31] Ze Liu, Yutong Lin, Yue Cao, Han Hu, Yixuan Wei, Zheng Zhang, Stephen Lin, and Baining Guo. Swin transformer: Hierarchical vision transformer using shifted windows. In *2021 IEEE/CVF International Conference on Computer Vision (ICCV)*, pages 9992–10002, 2021. doi: 10.1109/ICCV48922.2021.00986.
- [32] Wenhui Wang, Enze Xie, Xiang Li, Deng-Ping Fan, Kaitao Song, Ding Liang, Tong Lu, Ping Luo, and Ling Shao. Pyramid vision transformer: A versatile backbone for dense prediction without convolutions. In *Proceedings of the IEEE/CVF International Conference on Computer Vision*, pages 568–578, 2021.
- [33] Benjamin Graham, Alaaeldin El-Nouby, Hugo Touvron, Pierre Stock, Armand Joulin, Hervé Jégou, and Matthijs Douze. Levit: a vision transformer in convnet’s clothing for faster inference. In *Proceedings of the IEEE/CVF international conference on computer vision*, pages 12259–12269, 2021.
- [34] Ali Hassani, Steven Walton, Nikhil Shah, Abulikemu Abuduweili, Jiachen Li, and Humphrey Shi. Escaping the big data paradigm with compact transformers. 2021. URL <https://arxiv.org/abs/2104.05704>.
- [35] Sachin Mehta and Mohammad Rastegari. Mobilevit: Lightweight, general-purpose, and mobile-friendly vision transformer. *arXiv preprint arXiv:2110.02178*, 2021.
- [36] Zhou Wang, Alan C Bovik, Hamid R Sheikh, and Eero P Simoncelli. Image quality assessment: from error visibility to structural similarity. *IEEE transactions on image processing*, 13(4):600–612, 2004.
- [37] Wenzhe Shi, Jose Caballero, Ferenc Huszár, Johannes Totz, Andrew P Aitken, Rob Bishop, Daniel Rueckert, and Zehan Wang. Real-time single image and video super-resolution using an efficient sub-pixel convolutional neural network. In *Proceedings of the IEEE conference on computer vision and pattern recognition*, pages 1874–1883, 2016.
- [38] Dan Hendrycks and Kevin Gimpel. Gaussian error linear units (gelus). *arXiv preprint arXiv:1606.08415*, 2016.
- [39] Ilya Loshchilov and Frank Hutter. Sgdr: Stochastic gradient descent with warm restarts. *arXiv preprint arXiv:1608.03983*, 2016.
- [40] Adam Paszke, Sam Gross, Francisco Massa, Adam Lerer, James Bradbury, Gregory Chanan, Trevor Killeen, Zeming Lin, Natalia Gimelshein, Luca Antiga, et al. Pytorch: An imperative style, high-performance deep learning library. *Advances in neural information processing systems*, 32, 2019.
- [41] Olaf Ronneberger, Philipp Fischer, and Thomas Brox. U-net: Convolutional networks for biomedical image segmentation. In *International Conference on Medical image computing and computer-assisted intervention*, pages 234–241. Springer, 2015.
- [42] Christian Ledig, Lucas Theis, Ferenc Huszár, Jose Caballero, Andrew Cunningham, Alejandro Acosta, Andrew Aitken, Alykhan Tejani, Johannes Totz, Zehan Wang, et al. Photo-realistic single image super-resolution using a generative adversarial network. In *Proceedings of the IEEE conference on computer vision and pattern recognition*, pages 4681–4690, 2017.